Crystal structures of $(Mg_{1-x},Fe_x)SiO_3$ postperovskite at high pressures

Takamitsu Yamanaka[a], Kei Hirose[b], Wendy L. Mao[c,d], Yue Meng[e], P. Ganesh[a,1], Luke Shulenburger[a,2], Guoyin Shen[e], and Russell J. Hemley[a,3]

[a]Geophysical Laboratory, Carnegie Institution of Washington, Washington, DC 20015; [b]Department of Earth and Planetary Sciences, Tokyo Institute of Technology, Meguro, Tokyo 152–8551, Japan; [c]Department of Geological and Environmental Sciences, Stanford University, Stanford, CA 94305; [d]Photon Science, SLAC National Accelerator Laboratory, Menlo Park, CA 94025; and [e]High Pressure Collaborative Access Team, Geophysical Laboratory, Carnegie Institution of Washington, Argonne, IL 60439

Contributed by Russell J. Hemley, November 3, 2011 (sent for review May 9, 2011)

X-ray diffraction experiments on postperovskite (ppv) with compositions $(Mg_{0.9}Fe_{0.1})SiO_3$ and $(Mg_{0.6}Fe_{0.4})SiO_3$ at Earth core-mantle boundary pressures reveal different crystal structures. The former adopts the $CaIrO_3$-type structure with space group *Cmcm*, whereas the latter crystallizes in a structure with the *Pmcm* (*Pmma*) space group. The latter has a significantly higher density ($\rho = 6.119(1)$ g/cm^3) than the former ($\rho = 5.694(8)$ g/cm^3) due to both the larger amount of iron and the smaller ionic radius of Fe^{2+} as a result of an electronic spin transition observed by X-ray emission spectroscopy (XES). The smaller ionic radius for low-spin compared to high-spin Fe^{2+} also leads to an ordered cation distribution in the M1 and M2 crystallographic sites of the higher density ppv structure. Rietveld structure refinement indicates that approximately 70% of the total Fe^{2+} in that phase occupies the M2 site. XES results indicate a loss of 70% of the unpaired electronic spins consistent with a low spin M2 site and high spin M1 site. First-principles calculations of the magnetic ordering confirm that *Pmcm* with a two-site model is energetically more favorable at high pressure, and predict that the ordered structure is anisotropic in its electrical and elastic properties. These results suggest that interpretations of seismic structure in the deep mantle need to treat a broader range of mineral structures than previously considered.

diamond anvil cell | Earth's mantle | silicates

Since the discovery of $CaIrO_3$-structured $MgSiO_3$ postperovskite (ppv) (1, 2), numerous high-pressure-temperature (*P-T*) experiments and theoretical calculations have been performed to examine its role in explaining observations in the lowermost portions of the Earth's mantle. In this region of the planet, anomalous features have been documented by seismology, including the ultralow velocity zones (ULVZ) which have been attributed to partial melt, chemical and thermal heterogeneities (3, 4). Numerous studies of pure Mg (or Mg-rich) ppv have been undertaken to interpret these unusual seismic signatures (2, 5–13). Iron is likely to be an important component in ppv, and its incorporation in silicate ppv has been found to have a considerable influence on the properties of the phase. Experimental studies have demonstrated that ppv can take up much more iron than silicate perovskite (pv) (14, 15), and the equation of state (EOS) and phase boundaries have been determined as a function of Fe^{2+} content (16–19). In Al-bearing ppv, the presence of Fe^{3+} may also have a significant effect on the physical properties, phase boundaries and iron partitioning (20). Iron-rich ppv was found to have a very low shear wave velocity and high Poisson's ratio that may provide an alternate explanation for the origin of ULVZ (21). Spin transitions in iron-bearing ppv investigated using X-ray emission spectroscopy (XES) indicate that Fe^{2+} in ppv may have an intermediate spin state (22). Calculations also predict that the cation ordering and spin state have a significant effect on phase stability and EOS (23, 24).

Determining Fe and Mg cation distribution and ordering in $(Mg,Fe)SiO_3$-ppv is thus crucial for constraining the major element chemistry in the lowermost mantle. For example, element partitioning is strongly influenced by the relative cation sizes and compressibilities, and this in turn affects the EOS and other elastic properties. Previous structure refinements for $(Mg_{0.91}Fe_{0.09})SiO_3$-ppv based on in situ high *P-T* X-ray diffraction (XRD) measurements agree well with first-principles calculations for the Mg endmember (25) whereas iron-rich En60-ppv was found to have a different structure due to cation ordering (26). Here we report studies of the structure and electronic properties of $(Mg,Fe)SiO_3$-ppv with varying iron compositions using XRD, XES, and first-principles calculations. The refinement of $(Mg_{0.6}Fe_{0.4})SiO_3$-ppv reveals a *Pmcm* structure distinct from the *Cmcm* structure of $(Mg_{0.9}Fe_{0.1})SiO_3$-ppv and has a nonisomorphic subgroup symmetry of *Cmcm*. This information is important for understanding the origin of the physical properties of $(Mg,Fe)SiO_3$-ppv solid solutions, including anisotropy in elasticity and electrical conductivity and the relationship of these properties to seismic velocities. The results are used to examine the cation ordering, enthalpy, and magnetic spin ordering, which are important for modeling the Earth's lowermost mantle.

Results

X-ray Diffraction. We collected powder XRD patterns resulting from an average of many separate measurements for $(Mg_{0.9}Fe_{0.1})SiO_3$-ppv [90% enstatite (En)–10% ferrosilite (Fs), hereafter designated En90-ppv] at 131 GPa quenched from 2,000 K at BL10XU of SPring-8 and $(Mg_{0.6}Fe_{0.4})SiO_3$-ppv (hereafter designated En60-ppv) at 137 GPa quenched from 2,000 K at 13-ID-D of the Advanced Photon Source (APS). The diffraction patterns based on Rietveld profile fitting of En60-ppv and En90-ppv are presented in Figs. 1 and 2, respectively. The reliability factors of R_I, R_F, R_p, wR_p, and s of the refinements for En60-ppv indicate that the *Pmcm* model gives much better results than *Cmcm*. The atomic positions and temperature factors for both compositions are presented in Table 1. As seen from the calculated diffraction patterns based on both Rietveld analyses (Fig. S1), the primitive lattice of *Pmcm* allows several forbidden reflections such as 011, 031, 120, 013, and 033 that are forbidden in *Cmcm*. The relative intensities of the 020, 022, 110, and 111 reflections differ in the observed diffraction patterns. The inten-

Author contributions: T.Y., W.L.M., and R.J.H. designed research; T.Y., K.H., W.L.M., P.G., L.S., G.S., and R.J.H. performed research; Y.M. contributed new reagents/analytic tools; T.Y., K.H., W.L.M., Y.M., P.G., and L.S. analyzed data; and T.Y., K.H., W.L.M., P.G., L.S., and R.J.H. wrote the paper.

The authors declare no conflict of interest.

[1]Present address: Center for Nanophase Materials Sciences, Oak Ridge National Laboratory, Oak Ridge, TN 37830.

[2]Present address: Sandia National Laboratory, Albuquerque, NM 87185.

[3]To whom correspondence should be addressed. E-mail: hemley@gl.ciw.edu.

This article contains supporting information online at www.pnas.org/lookup/suppl/doi:10.1073/pnas.1118076108/-/DCSupplemental.

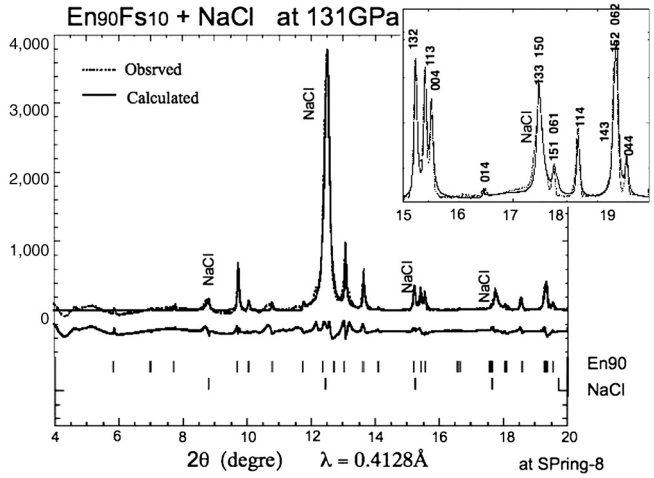

Fig. 1. Rietveld XRD profile fitting of En90-ppv and NaCl. The observed XRD pattern and the fitted pattern based on the *Cmcm* model are shown by dotted and solid lines, respectively. The residual fitting error is presented by the solid line in the lower trace. The observed pattern was made by averaging ten patterns collected from different sample positions at 131 GPa and ambient temperature after laser heating to 2,000 K. The upper right figure shows the enlarged pattern from 15° to 20°; the reliability factors are: $R_{wp} = 0.79$, $R_p = 0.54$, $s = 0.596$, En90: $R_I = 8.16$, $R_F = 3.81$, NaCl: $R_I = 3.63$, $R_F = 3.28$.

sity difference between En90 and En60 are shown in the enlarged portion of diffraction patterns of both figures.

The observed patterns for En90 and En60-ppv are very similar. However, the peak intensities and several extra peaks not allowed by a C-lattice are found in En60-ppv; these are very weak but detectable above the noise level. The diffraction patterns are calculated from Rietveld refinements for En90 (*Cmcm*), En60 (*Pmcm*), and ideal En50 (*Pmcm*) (see *SI Text*). The last is based on a fully ordered model of $Mg_{0.5}Fe_{0.5}SiO_3$ with the M1 site fitted by Mg and M2 site by Fe. En60 has different site occupancies for M1 ($Mg_{0.75}Fe_{0.25}$) and M2 ($Mg_{0.45}Fe_{0.55}$), indicating a partially ordered structure in which 70% of Fe occupies the M2 site. The different relative diffraction intensities are attributable to cation ordering. Key differences in the results for En90

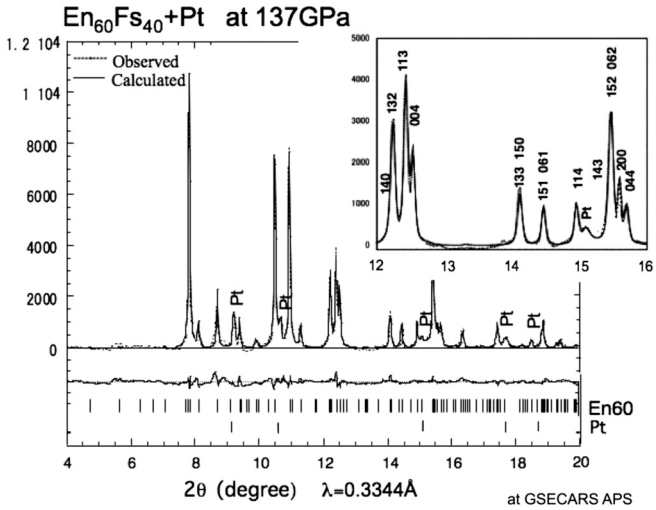

Fig. 2. Rietveld XRD analysis of En60-ppv patterns and Pt showing the observed (dotted line) and fitted using the *Pmcm* model (solid line). XRD pattern was collected at 137 GPa and ambient temperature from more than 20 patterns at different sample positions and angles after laser heating to 2,000 K. The upper right figure shows the enlarged pattern from 12° to 16°. The reliability factors are: $R_{wp} = 0.18$, $R_p = 0.12$, $s = 0.443$, En60: $R_I = 6.64$, $R_F = 5.55$, Pt: $R_I = 7.43$, $R_F = 3.40$.

Table 1. Positional parameters and temperature factors

En60, space group *Pmcm* (SG = 51), $Z = 4$*

Atom	Wyc	g	x	y	z	B
M1	2*e*	1.17(11)	0.25	0.0	0.253(4)	2.3(1.7)
M2	2*f*	0.891(8)	0.25	0.5	0.752(3)	1.7(0.9)
Si1	2*a*	1.0	0.0	0.0	0.0	2.2(0.8)
Si2	2*d*	1.0	0.0	0.5	0.5	1.8(0.7)
O1	2*e*	1.0	0.25	0.0	0.925(9)	2.1(0.8)
O2	2*f*	1.0	0.25	0.5	0.433(7)	0.8(0.9)
O3	4*i*	1.0	0.441(4)	0.0	0.637(3)	1.1(0.9)
O4	4*i*	1.0	0.437(8)	0.5	0.121(3)	2.2(1.3)

En90, space group *Cmcm* (SG = 63), $Z = 4$†

Atom	Wyc	g	x	y	z	B
M	4*c*	1.0	0.0	0.260(1)	0.25	1.11(4)
Si	4*a*	1.0	0.0	0.0	0.0	0.96(4)
O1	4*c*	1.0	0.0	0.932(2)	0.25	2.05(4)
O2	8*f*	1.0	0.0	0.645(1)	0.445(2)	0.30(3)

*$R_I = 6.64$, $R_F = 5.55$, $R_{wp} = 0.18$, $R_p = 0.12$, $s = 0.443$. Site occupancy: M1 ($Mg_{0.75}Fe_{0.25}$), M2 ($Mg_{0.45}Fe_{0.55}$), $a = 2.4648(8)$, $b = 8.1529(6)$, $c = 6.1252(2)$, Vol = 123.09(2).

†$R_I = 8.16$, $R_F = 3.81$, $R_{wp} = 0.79$, $R_p = 0.54$, $s = 0.596$. Site occupancy: M ($Mg_{0.90}Fe_{0.10}$), $a = 2.4597(7)$, $b = 8.0505(29)$, $c = 6.1051(14)$, Vol = 120.89(6).

and En60 are highlighted in the enlarged portions of Figs. 1 and 2.

Monte Carlo calculations using the diffraction intensities of En60-ppv led to four candidate structures, all belonging to nonisomorphic subgroups of *Cmcm*. These structures have two distinct metal sites: *Pmmn* (*Pmnm*), *Pm2m* (*Pmm2*), and *Cm2m* with (M1,M2)SiO_3, and *Pmcm* (*Pmma*). The converged lattice parameters of En90-ppv with *Cmcm* are $a = 2.4597(7)$ Å, $b = 8.0505(29)$ Å, $c = 6.1051(14)$ Å, $V = 120.89(6)$ Å^3, and $\rho = 5.694(8)$ g/cm^3. Those for En60-ppv with *Pmcm* are $a = 2.4648(3)$ Å, $b = 8.1529(10)$ Å, and $c = 6.1252(7)$ Å, $V = 123.09(3)$ Å^3. Making a small correction for the difference in pressure using the EOS of En60-ppv (21) gives $\rho = 6.119(1)$ g/cm^3 for 131 GPa. Having Fe and Mg cations randomly distributed on one site gives rise to space group *Cmcm*. This structure has one crystallographically equivalent site. In contrast, the *Pmcm* model has two different M sites, M1 and M2, on which the Mg and Fe cations are partially ordered. The difference in the scattering factors between Fe^{2+} and Mg^{2+} is large enough to resolve the degree of ordering on the metal sites. The diffraction intensity for each *hkl* reflection is related to the structure factor, which in turn is a function of the site occupancy and atomic scattering factor. The *Pmcm* structure with variable site occupancy (*g*) on these two sites yields noticeable differences in diffraction intensities. The site occupancies of En60-ppv were found to be ($Mg_{0.75}Fe_{0.25}$) and ($Mg_{0.45}Fe_{0.55}$) for the M1 and M2 sites, respectively with about 70% of the total Fe atoms located on the M2 site. The Si atoms were also located on two crystallographically independent sites.

The average bond distance at the M1 site is larger than that of M2 in En60-ppv (Table 2). These two sites are arranged in a zigzag fashion along the *b* and *c* axes, as seen in Fig. 3. Considering the empirical ionic radii of high-spin (HS) Fe^{2+} ($r_{Fe} = 0.92$ Å) and Mg^{2+} ($r_{Mg} = 0.89$ Å) in the eightfold coordination site at ambient conditions (27), one might expect that the larger M1 site would be preferentially occupied by Fe^{2+} and the smaller M2 site by Mg^{2+}. However, the structure refinement indicates a preferential occupancy of Mg^{2+} in the larger M1 site and Fe^{2+} in the smaller M2 site. This points to the role of different electronic spin states in controlling the structure, which we clarified using XES.

X-ray Emission Spectroscopy (XES). The excitations probed by XES can be described by a two-step (absorption followed by emission)

Table 2. Bond distances (Å)

En60 at 137 GPa, *Pmma* (SG = 51), $Z = 4$

$a = 6.1252(7)$, $b = 2.4648(3)$, $c = 8.1529(10)$, Vol = 123.088(9)

M1 site	$Fe_{0.25}$, $Mg_{0.75}$	M2 site	$Fe_{0.55}$, $Mg_{0.45}$	Si1 site		Si2 site	
8-fold	2e *mm*2	8-fold	2*f mm*2	6-fold	2*a* .2/*m*	6-fold	2*d* .2/*m*
O2 × 2	1.910	O1 × 2	1.855	O1 × 2	1.614	O2 × 2	1.623
O4 × 4	2.013	O3 × 4	1.934	O4 × 4	1.661	O3 × 4	1.715
O3 × 2	2.063	O4 × 2	2.207				
Av	2.000	Av	1.982	Av	1.645	Av	1.684
O1 site		O2 site		O3 site		O4 site	
4-fold	2e *mm*2	4-fold	2e *mm*2	5-fold	4*i* .*m*.	5-fold	4*i* .*m*.
Si1×	1.661	Si2 × 2	1.623	Si2 × 2	1.715	Si1 × 2	1.614
M2 × 2	1.855	M1 × 2	1.910	M1 × 2	1.934	M2 × 2	2.03
				M2 × 1	2.063	M1 × 1	2.207
Av	1.758	Av	1.766	Av	1.872	Av	1.892

En90 at 131 GPa, *Cmcm* (SG = 63), $Z = 4$

$a = 2.4597(7)$, $b = 8.0505(29)$, $c = 6.1051(14)$, Vol = 120.89(6)

M site	$Mg_{0.90}Feg_{0.10}$	Si site		O1 site		O2 site	
8-fold	4*c m*2*m*	6-fold	4*a* 2/*m*.	4-fold	4*c m*2*m*	5-fold	8*f m*.
O2 × 2	1.850	O1 × 2	1.621	S1 × 2	1.621	S1 × 2	1.726
O4 × 4	1.949	O3 × 4	1.726	M × 2	1.850	M × 2	1.949
O3 × 2	2.015					M × 1	2.015
Av	1.940	Av	1.691	Av	1.736	Av	1.873

model. $K\beta$ emission results from a transition from 3*p* to 1*s*. A 3*p* electron then falls into the ground state accompanied by the emission of a $K\beta$ photon. In the final state the 3*p* core hole interacts strongly with the partially filled 3*d* shell. This leads to the characteristic splitting observed in the XES spectra for iron compounds which have a higher energy main peak of $K\beta_{1,3}$ and the HS state a lower energy satellite peak of $K\beta'$. The intensity of the $K\beta'$ satellite peak follows the variations in the spin state of the material. The loss of $K\beta'$ indicates the collapse of the 3*d* magnetic moment and a transition from HS to LS.

The XES spectrum of En60-ppv at 124 GPa, synthesized from the same orthopyroxene starting material used in the XRD experiments, is consistent with a mixed spin state in which 70% of the total Fe transforms to LS and 30% remains in HS (Fig. 4). The spin transition from HS to LS reduces the Fe^{2+} ionic radius in the eightfold coordinated site by about 10% (27): $r_{Fe} = 0.92$ Å (HS) and $r_{Fe} = 0.74$ Å (LS) for ambient conditions; the Mg ion at the same site is $r_{Mg} = 0.89$ Å. A larger amount of LS Fe^{2+} occupies the smaller M2 site due to its smaller ionic radius, consistent with the Rietveld refinement. The average bond distances for the two metal sites (Table 2) are consistent with the HS Fe^{2+} in the M1 site and LS Fe^{2+} in the M2 site.

First-Principles Calculations. We performed density functional theory (DFT) calculations to investigate the stability and properties of the *Pmcm* postperovskite. We considered two different ordered structures for $(Mg_{0.5}Fe_{0.5})SiO_3$-ppv: *Pmcm* with Fe atoms are placed on the M2 sites and Mg on the M1 sites and *Pm*2*m* with equal amounts of Fe and Mg atoms in both sites; the latter is similar to the *Cmcm* structure with Fe and Mg atoms are distributed equally resulting in only one distinct site. We performed full geometry optimization for both ferromagnetic and antiferromagnetic electronic symmetries at a series of volumes to give the full EOS (Fig. 5). We found that the antiferromagnetic spin symmetry has a lower energy for all pressures. At 137 GPa the enthalpy of the phase with Fe only on M2 was approximately 50 meV per 20-atom cell lower than the phase with equal amounts of Fe on both sites. As the energy differences are small, a separate calculation was performed in VASP (29–31) to quantify the dependence of this small quantity on the algorithm and the pseudopotentials. The static enthalpy difference for our optimized structure was found to be approximately 40 meV per 20-atom cell with a smaller plane-wave cutoff energy of approximately 500 eV, consistent with our findings with ABINIT. A fully relaxed calculation at 137 GPa gave a slightly lower enthalpy difference of approximately 30 meV per 20-atom cell. Optimized coordinates are given in Table S3.

Using this result we constructed a simple model taking into account nearest neighbor interactions of Fe for the enthalpy as a function of the site occupancy in En60: $\Delta H(x) = 0.8x(1-x)$ (0.2 eV) per unit cell and $\Delta S = 2k_B[x\ln x + (1-x)\ln(1-x) + (0.8-x)\ln(0.8-x) + (0.2+x)\ln(0.2+x)]$, where x is the fraction of Fe on M2. We then calculated ΔG for the transformation of En60-ppv from *Cmcm* to *Pmcm*, finding a transition at 278 K. This is consistent with the experimental interpretation of a *Pmcm* structure for En60-ppv measured at 137 GPa and room temperature. The calculated transition temperature is too low to have direct

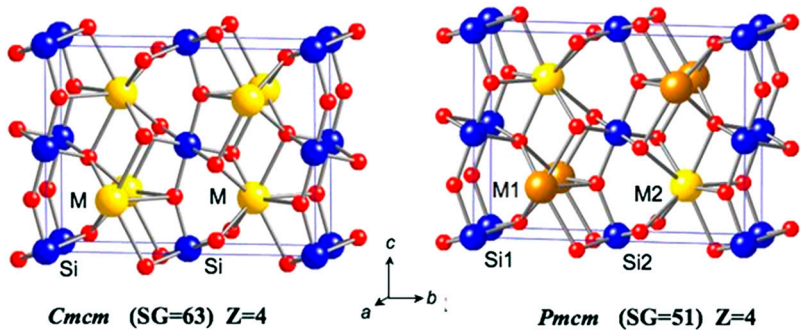

Fig. 3. Structure of En90-ppv with space group *Cmcm* and En60-ppv with *Pmcm*. Red atoms: O^{2-}; blue: Si^{4+}; brown: M1 site = $(Fe^{2+}{}_{0.25}Mg^{2+}{}_{0.75})$; yellow: M2 site = $(Fe^{2+}{}_{0.55}Mg^{2+}{}_{0.45})$.

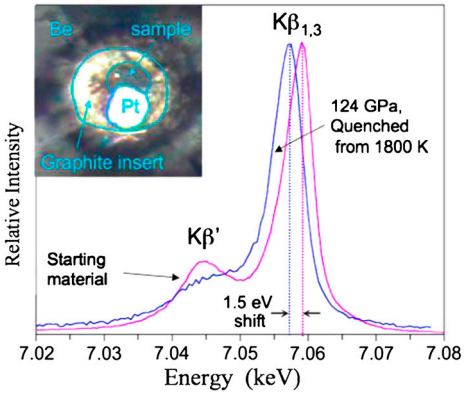

Fig. 4. Fe $K\beta$ X-ray emission spectrum for En60-ppv showing 70% intensity loss in $K\beta'$ in ppv compared to the starting material.

geophysical implications, but warrants further investigation using more realistic models of the disordered phase.

Calculations over a wide range of pressures allowed us to extract the magnetic moment of the ground state antiferromagnetic spin structure for both the *Pmcm* and the *Pm2m* phases. They reveal HS to LS transition pressures for the two different structures that differ by approximately 200 GPa (Fig. 5). The result indicates the importance of site ordering in predicting spin transitions. A fit to a Vinet EOS (Table S2) suggests that the bulk modulus of the two phases in their LS state differ by about 10 GPa, whereas their HS states have similar values. Because the Fe *d*-electrons are thought to be strongly localized but also take part in bonding due to their itinerancy, DFT + U calculations were performed for the experimental *Pmcm* structure with $U = 8$ eV and $J = 1$ eV using the fully-localized limit for the double-counting (32). In the antiferromagnetic state, we found *Pmcm* to be more stable than the model for *Cmcm*. With a lower value of $U = 4.5$ eV, the enthalpy difference between the two phases dropped slightly to 41 meV/unit cell. We further performed constrained orbital occupation calculations and found that the HS state was more stable than the LS or intermediate-spin states. These calculations directly support the experimental findings of a unique structure in which the Fe atoms prefer to be in nonequivalent sites, thereby reducing the overall symmetry from *Cmcm* to *Pmcm*. A separate DFT calculation was further performed on the *Pmcm* phase; one with magnetic (HS) Fe atoms and the other with nonmagnetic (LS) Fe atoms at a constant pressure of 137 GPa. The equilibrium volume of the HS structure was slightly larger than that of the nonmagnetic structure. A large part (approximately 50%) of this volume change was due to the increased polyhedral volume around the HS Fe atoms clearly indicating that HS Fe prefers a larger local polyhedron compared to a LS Fe in iron-magnesium silicate.

LAPW calculations (33) were performed for the optimized *Pmcm* structure to predict the XES spectrum (34) for HS and LS (nonmagnetic) state in an antiferromagnetic spin-arrangement (Fig. 6). The XES spectrum (shifted by approximately −0.1 eV for the minority spin and approximately 0.28 eV for the LS state) of the majority-spin in the HS state shows a prominent low-energy shoulder (approximately −10.3 eV), which is greatly reduced for the minority-spin as well as for LS Fe. This agrees with the experimental observation of a reduced low-energy shoulder for the spectrum of the *Pmcm* phase, indicating of a HS to LS transition. The inset of Fig. 6 also compares the atom projected partial density of states (*p*-DOS) of Fe as well as the radial transition probabilities for the LS transition. The transition probabilities are larger for the LS state compared to HS states, but the reduction in the computed low-energy peak appears to be mainly due to a reduced *p*-DOS of the LS (minority-spin) configuration at that energy.

Discussion

Our XRD and XES results are consistent with previous synchrotron Mössbauer measurements (22) that show two predominant sites in the En60-ppv spectrum at 134 GPa, consistent with our two-site model. On the other hand, En90-ppv has relatively low iron content and does not show an obvious cation ordering. Consequently, there is no resolvable difference in the cation site, and En90-ppv is well described by the *Cmcm* structure and only one cation site. Our first-principles calculations show that changing the site occupancies such that M1 is depleted in iron relative to M2 lowers the enthalpy of the ppv structure consistent with the experimental findings. Both Fe on M2 (*Pmcm*) arranged with alternating up and down spins was 50 meV per 20-atom cell lower than the configuration where the Fe is located on both sites (*Pm2m*). This is consistent with the experimental interpretation of a *Pmcm* structure of ppv. The calculation leads to a structure that is very similar to that obtained from the profile fitting. Mg and Fe are randomly distributed in the *Cmcm* structure but ordered in *Pmcm*. Anisotropy in the elasticity and electrical properties of the ppv is expected from the changes in spin-transition pressures (Fig. 5) and bulk moduli (Table S2), but further experimental and theoretical studies are required to quantify these effects. Notably, En90-ppv does not appear to exhibit this anisotropy; this may be due to its lack of cation ordering.

In conclusion, XRD/Rietveld analysis, XES measurements, and first-principles calculations together with published Mössbauer measurements (22) show that $(Mg_{1-x},Fe_x)SiO_3$-ppv yields ground-state structures that differ from those previously considered. A two-site crystallographic model is required for iron-rich ppv, and the iron in the material exists in two distinct forms, one in the LS state on the M2 site and the other in a HS state on the M1 site. Consequently, the phase boundaries and other physical

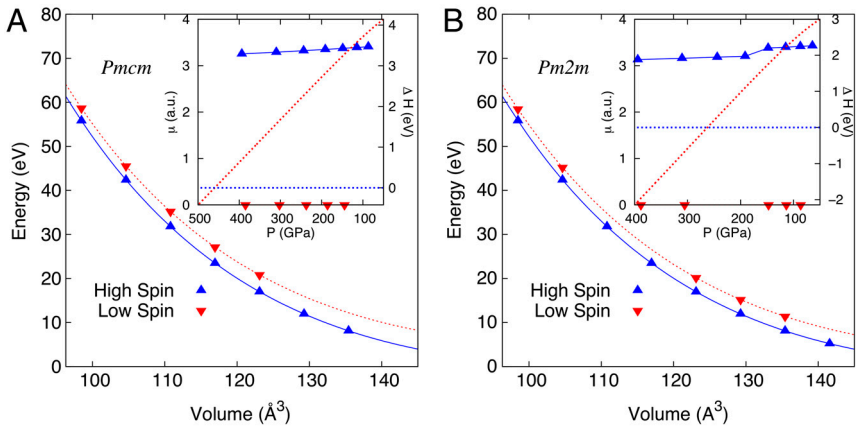

Fig. 5. Spin transition and EOS for the antiferromagnetic *Pmcm* (*A*) and *Pm2m* (*B*) phases. The main figures show the energy vs. volume for the relaxed structures. The points in the inset show the magnetic moment on the Fe atoms in atomic units (Bohr magneton) as a function of pressure with the scales on the left axis. The lines in the inset show the enthalpy difference between the HS and LS phases compared to the HS phase with the scale on the right axis. The discontinuity in the magnetic moment of the *Pm2m* phase is due to uncertainty in the predicted quantity.

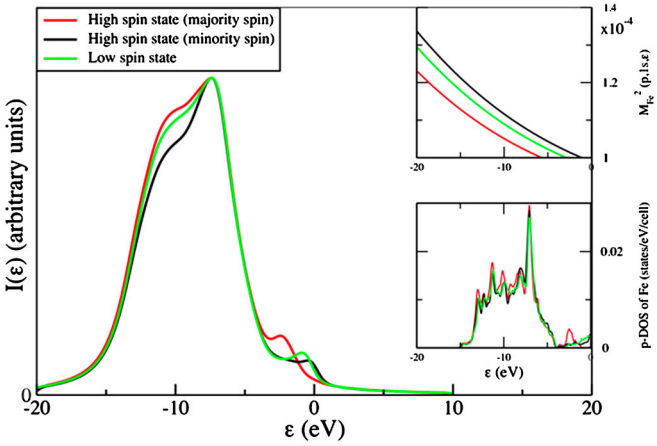

Fig. 6. Computed theoretical XES Fe-*K* edge spectrum in *Pmcm* symmetry with Fe in LS and in the HS states. ε is the emitted X-ray energy with respect to the Fermi level (shifted by an additional approximately −0.1 eV for the minority spin and approximately 0.28 eV for the LS state to match the main peak). Insets show the radial transition probabilities (M_{Fe}) for the $3p \rightarrow 1s$ transition as well as the partial atom projected partial density of states (*p*-DOS).

properties of $(Mg_{1-x},Fe_x)SiO_3$-ppv are expected to be affected by the HS to LS spin transition.

Experimental Methods

Sample Preparation. Synthetic En60-ppv starting material was prepared as described previously (15). Fine powder was loaded into diamond anvil cells (DACs) containing beveled diamonds with 90 μm culets and a 450 μm outer diameter together with platinum metal as a the pressure marker. No pressure-transmitting medium was used. A Re gasket was preindented to 30 μm and drilled to make a 40-μm diameter sample chamber. The sample was heated by a double-sided Nd:YLF laser-heating system. Temperature was determined to be approximately 2,000 K using spectral radiometry. En90-ppv was synthesized from a gel in laser-heated DACs. The gel starting material was completely dehydrated beforehand at 1,273 K in a H_2-CO_2 gas-mixing furnace, in which oxygen fugacity was controlled slightly above the iron-wüstite buffer. The sample was loaded together with a NaCl pressure medium into a 50 μm hole in a preindented Re gasket. Beveled diamond anvils with 150 μm culet were used for compression. The sample was heated to approximately 2,000 K for approximately 10 min by Nd:YLF laser at BL10XU, SPring-8.

X-ray Diffraction. The angle-dispersive powder XRD measurements on En60-ppv were performed at 13-ID-D, GSECARS, of the Advanced Photon Source (APS) with $\lambda = 0.3344$ Å. Powder diffraction patterns were collected on charge-coupled device (CCD) detector. To avoid reaction with the gasket and Pt pressure calibrant, we were careful to not heat the Pt and gasket, and did not see evidence for additional Pt-alloys or carbide. The laser heating helped relieve deviatoric stresses especially at the center of the heated spot where the XRD data was collected. A variation in the intensities of Debye-Scherrer rings was observed as a result of preferred orientation and differential stress on the sample; in addition, grain growth on synthesis resulted in spottiness and nonuniformity of the powder rings. Twenty XRD patterns collected at different χ and ω angles and X-ray beam positions were averaged until they converged (i.e. the peak intensity did not vary with more sampling) to create one powder pattern. The iron-rich En60 composition was particularly useful for differentiating cation positions because Fe^{2+} has six times the higher scattering intensity compared to Mg^{2+}, Si^{4+} and O^{2-} that all have 10 e^-. Consequently we collected twenty powder diffraction patterns taken from different positions in the gasket hole and at the several omega angles using a 5 × 5 μm beam. After the data reduction of all datasets, we added the diffraction intensities of all spectra and created one powder pattern. The standard deviation of the intensity data of $I(hkl)$ was determined to be less than 3%. The angle-dispersive XRD pattern for En90 ppv was collected at BL10XU, SPring-8 on an imaging plate detector (35). We used a monochromatic X-ray beam with $\lambda = 0.41282$ Å and averaged ten spectra. The 2D diffraction image showed that the Debye rings are not spotty but have quite uniform intensity.

Rietveld profile fitting was conducted by the program RIETAN-2000 (36). To fit the data, first the background intensity distribution was adjusted for the refinement. Then lattice constants, atomic coordinates and temperature factors were treated as variable parameters; profile parameters and site-occupancy parameters were varied in the refinement. Finally a full matrix least-squares refinement was conducted. The results for the full width at half maximum (FWHM), asymmetry parameters, and peak profile function confirm that the diffraction data show the reliability of the profile analysis. The site-occupancy was refined and conducted using only one variable parameter for Fe, Fe(M2) at M2. The rest of the site occupancies were then determined based on the bulk chemical constraint for En60, yielding Mg(M2) = 1.0-Fe(M2), Fe(M1) = 0.8-Fe(M2) and Mg(M1) = 0.2 + Fe(M1). The site occupancy refinements as a function of mixing ratio of Fe and Mg are presented in Table S1. The refinement for $(Mg_{0.75}Fe_{0.25})$ and $(Mg_{0.45}Fe_{0.55})$ at the M1 and M2 sites show the highest reliability factors of R_F and R_I. Furthermore, the *g*-value converged to a reasonable value of $g = 1.0$ in both sites, because $g < 1$ indicates the cation vacancy due to the defect and $g > 1$ is an interstitial distribution by the excess cation (Fig. S2).

The definitions of the reliability factors R_F, R_I, R_P, wR_P and goodness of fit s in the refinement are

$$R_F = \left[\frac{\Sigma_k |F_{k\,\mathrm{obs}}| - |F_{k\,\mathrm{cal}}|}{\Sigma_k F_{k\,\mathrm{obs}}}\right], \qquad R_I = \left[\frac{\Sigma_i |I_{i\,\mathrm{obs}} - I_i(x)|}{\Sigma_i I_{i\,\mathrm{obs}}}\right],$$

$$R_P = \left[\frac{\Sigma_i |y_i - f_i(x)|}{\Sigma_i y_i}\right], \qquad wR_p = \left[\frac{\Sigma_i w_i |y_i - f_i(x)|}{\Sigma_i w_i y_i}\right]^{1/2},$$

$$s = \left[\frac{\Sigma_i w_i |y_i - f_i(x)|}{N - P}\right]^{1/2}$$

where I and F indicate the integrated intensity of diffraction peak and structure factor, respectively. y_i is the observed diffraction intensity at i'th position in 2θ, $f(x)$ is the calculated intensity. N and P are the total number of the data points and variable parameters, respectively; w is a weight for the data points.

X-ray Emission Spectroscopy (XES). XES experiments were performed at 16-ID-D of the High Pressure Collaborative Access Team (HPCAT) of the APS. The incident X-ray beam was passed through a diamond monochromator that selects an X-ray energy above the Fe *K* absorption edge. The beam was then focused to 60 μm horizontal × 20 μm vertical using a pair of Kirkpatrick–Baez mirrors which allowed selection of the area probed to be restricted to the small sample chamber, thereby minimizing possible scattering from the diamond cell or impurities in the gasket. The Fe-*K*β emission from the sample was collected through the gasket to avoid attenuation by diamond and hits the Si (333) analyzer crystal that sits along with the detector on a high resolution (0.5 eV) Rowland-circle spectrometer. The analyzer was positioned perpendicular to the incident X-rays to reduce background from elastic scattering. Energy was scanned by changing the analyzer θ (and detector 2θ). The En60 sample in a 100-μm in diameter graphite gasket was inserted inside an X-ray transparent Be gasket and compressed to 124 GPa. The graphite converted to a transparent, superhard high-pressure phase that helps maintain sample thickness and is also thermally insulating to prevent the gasket from being heated (37). A small piece of Pt was added

as a pressure standard that was compressed between the sample and one of the diamond culets. The sample was heated to 1,800 K and then quenched to ambient temperature for the XES measurements.

Density Functional Calculations. First-principles calculations based on the spin polarized generalized gradient approximation (GGA) (28) of density functional theory (DFT) (38, 39) were performed using the ABINIT (40, 41) package for 20-atom orthorhombic unit cells (42). The convergence parameters were increased until the energies calculated converged to within 0.1 mHa, yielding a kinetic energy cutoff for the plane waves of 70 Ha, a 140 Ha cutoff for the matching grid and a $6 \times 6 \times 6$ grid of **k**-points. The electronic configurations for the valence band states for Fe, Mg, Si, and O are $3s^2 3p^6 3d^6$, $2s^2 2p^6 3s^2$, $2s^2 2p^6 3s^2 3p^2$, and $2s^2 2p^4$, respectively, and the cutoff distances for the projector augmented wave (PAW) potentials are 1.7, 1.9, 1.5, and 1.4 Bohr. In each calculation the geometry was relaxed while preserving the symmetry of the underlying structure.

LAPW calculations were performed on optimized structures in the *Pmcm* space group in HS and LS configurations to compute Fe-K XES spectra. Sphere radii for Fe, Mg, Si, and O were 1.96, 1.78, 1.51, and 1.51 a.u. respectively. A large RKMAX (matrix size) value of 9.0 was chosen. The cutoff for the potential and charge density was GMAX = 30 Ry. A $10 \times 10 \times 10$ **k**-mesh (125 **k**-points in irreducible Brillouin zone) was used. Brillouin zone integrations were conducted using a tetrahedron scheme. A spectrometer broadening of $S = 0.5$ eV, a core-state lifetime broadening of $\Gamma = 0.6$ eV and a valence-state broadening of $W = 0.5$ eV were chosen to compute spectra.

ACKNOWLEDGMENTS. We thank Y. Xiao, P. Chow, V. Prakapenka, and Y. Ohishi for help with the experiment; M. Phillips for her assistance in preparing the manuscript; H.K. Mao and R.E. Cohen for useful discussions; and the reviewers for comments on the paper. W.L.M. is supported by National Science Foundation (NSF) (EAR-0738873). GSECARS is supported by NSF (EAR-0622171) and US Department of Energy (DOE) (DE-FG02-94ER14466). The HPCAT facility is supported by the Carnegie Institution of Washington (CIW); the Carnegie/Department of Energy Alliance Center (CDAC); the University of Nevada, Las Vegas; and Lawrence Livermore National Laboratory (DE-FG02-99ER45775). Research performed at CIW is supported by DOE-Basic Energy Sciences, DOE-National Nuclear Security Administration (DE-FC52-08NA28554), and NSF (EAR-0911492). The APS is supported by the DOE-Basic Energy Sciences (DE-AC02-06CH11357).

1. Murakami M, Hirose K, Kawamura K, Sata N, Ohishi Y (2004) Post-perovskite phase transition in $MgSiO_3$. *Science* 304:855–858.
2. Oganov AR, Ono S (2004) Thoretical and experimental evidence for a post-perovskite phase of $MgSiO_3$ in Earth's *D″* layer. *Nature* 430:445–448.
3. Garnero EJ, McNamara AK (2008) Structure and dynamics of Earth's lower mantle. *Science* 320:626–628.
4. Lay T, Hernlund J, Garnero EJ, Thome M (2006) A post-perovskite lens and *D″* heat flux beneath the central pacific. *Science* 314:1272–1276.
5. Ballaran TB, Trønne RG, Frost DJ (2007) Equations of state of $CaIrO_3$ perovskite and post-perovskite phases. *Am Mineral* 92:1760–1763.
6. Iitaka T, Hirose K, Kawamura K, Murakami M (2004) The elasticity of the $MgSiO_3$ post-perovskite phase in the Earth's lowermost mantle. *Nature* 430:442–445.
7. Merkel S, et al. (2007) Deformation of $(Mg,Fe)SiO_3$ post-perovskite and *D″* anisotropy. *Science* 316:1729–1732.
8. Ono S, Oganov A (2005) In situ observations of phase transition between perovskite and $CaIrO_3$-type phase in $MgSiO_3$ and pyrolitic mantle composition. *Earth Planet Sc Lett* 236:914–932.
9. Tateno S, Hirose K, Sata N, Ohishi Y (2009) Determination of post-perovskite phase transition boundary up to 4,400 K and implications for thermal structure in *D″* layer. *Earth Planet Sc Lett* 277:130–136.
10. Tsuchiya T, Tsuchiya J, Umemoto K, Wentzcovitch RM (2004) Phase transition in $MgSiO_3$ perovskite in the Earth's lower mantle. *Earth Planet Sc Lett* 224:241–248.
11. Wentzcovitch RM, Tsuchiya T, Tsuchiya J (2006) $MgSiO_3$ postperovskite at *D″* conditions. *Proc Natl Acad Sci USA* 103:543–546.
12. Oganov AR, Martonák R, Raiteri AL, Parrinello M (2005) Anisotropy of Earth's *D″* layer and stacking faults in the $MgSiO_3$ post-perovskite phase. *Nature* 438:1142–1144.
13. Wookey J, Stackhouse S, Kendall J-M, Brodholt J, Price GD (2005) Efficacy of the post-perovskite phase as an explanation for lowermost-mantle seismic properties. *Nature* 438:1004–1007.
14. Mao WL, et al. (2005) Iron-rich silicates in the Earth's *D″* layer. *Proc Natl Acad Sci USA* 102:9751–9753.
15. Mao WL, et al. (2004) Ferromagnesian post-perovskite silicates in the *D″* layer of the Earth. *Proc Natl Acad Sci USA* 101:15867–15869.
16. Shieh SR, et al. (2006) Equation of state of the postperovskite phase synthesized from a natural $(Mg,Fe)SiO_3$ orthopyroxene. *Proc Natl Acad Sci USA* 103:3039–3043.
17. Mao WL, Mao HK, Prakapenka VB, Shu J, Hemley RJ (2006) The effect of pressure on the structure and volume of ferromagnesian post-perovskite. *Geophys Res Lett* 33:L12S02.
18. Sinmyo R, Hirose K, O'Neill HSC, Okunishi E (2006) Ferric iron in Al-bearing post-perovskite. *Geophys Res Lett* 33:L12S13.
19. Jackson JM, Sturhahn W, Tschauner O, Lerche M, Fei Y (2009) Behavior of iron in $(Mg,Fe)SiO_3$ post-perovskite assemblages at Mbar pressures. *Geophys Res Lett* 36: L10301.
20. Tschauner O, et al. (2008) Possible structural polymorphism in Al-bearing magnesium-silicate post-perovskite. *Am Mineral* 93:533–539.
21. Mao WL, et al. (2006) Iron-rich post-perovskite and the origin of ultralow-velocity zones. *Science* 312:564–565.
22. Lin JF, et al. (2008) Intermediate-spin ferrous iron in lowermost mantle post-perovskite and perovskite. *Nat Geosci* 1:688–691.
23. Caracas R, Cohen RE (2008) Ferrous iron in post-perovskite from first-principles calculations. *Phys Earth Planet In* 168:147–152.
24. Stackhouse S, Brodholt JP, Dobson DP, Price GD (2006) Electronic spin transitions and the seismic properties of ferrous iron-bearing $MgSiO_3$ post-perovskite. *Geophy Res Lett* 33:L12S03.
25. Shim S-H, et al. (2008) Crystal structure and thermoelastic properties of $(Mg_{0.91}Fe_{0.09})SiO_3$ postperovskite up to 135 GPa and 2,700 K. *Proc Natl Acad Sci USA* 105:7382–7386.
26. Yamanaka T, Mao WL, Hemley RJ, Shen G (2010) New structure and spin state of iron-rich $(Mg,Fe)SiO_3$ post-perovskite. *J Phys Conf Ser* 215:012100.
27. Shannon RD (1976) Revised effective ionic radii and systematic studies of interatomic distances in halides and chalcogenides. *Acta Crystallogr A* 32:751–767.
28. Perdew JP, Burke K, Emzerhoff M (1996) Generalized gradient approximation made simple. *Phys Rev Lett* 77:3865–3868.
29. Blöchl PE (1994) Projector augmented-wave method. *Phys Rev B* 50:17953–17979.
30. Kresse G, Furthmüller J (1996) Efficient iterative schemes for ab initio total-energy calculations using a plane-wave basis set. *Phys Rev B* 54:11169–11186.
31. Kresse G, Joubert D (1999) From ultrasoft pseudopotentials to the projector augmented-wave method. *Phys Rev B* 59:1758–1775.
32. Lichtenstein AI, Anisimov VI, Zaanen J (1995) Density-functional theory and strong interactions: Orbital ordering in Mott–Hubbard insulators. *Phys Rev B* 52:R5467–R5470.
33. Schwarz K, Blaha P, Madsen GKH (2001) Electronic structure calculations of solids using the WIEN2k package for material sciences. *Comput Phys Commun* 147:71–76.
34. Schwarz K, Neckel A, Nordgren J (1979) On the X-ray emission spectra from FeAl. *J Phys F Met Phys* 9:2509–2521.
35. Sata N, et al. (2010) Compression of FeSi, Fe_3C, $Fe_{0.95}O$, and FeS under the core pressures and implication for light element in the Earth's core. *J Geophys Res* 115:B09204.
36. Izumi F, Ikeda T (2000) A Rietveld-analysis program RIETAN-98 and its applications to zeolites. *Mater Sci Forum* 321–324:198–203.
37. Mao WL, et al. (2003) Bonding changes in compressed superhard graphite. *Science* 302:425–427.
38. Hohenberg P, Kohn W (1964) Inhomogeneous electron gas. *Phys Rev B* 136:B864–B871.
39. Kohn W, Sham LJ (1965) Self-consistent equations including exchange and correlation effects. *Phys Rev* 140:A1133–A1138.
40. Gonze X, et al. (2002) First-principles computation of material properties: The ABINIT software project. *Comp Mater Sci* 25:478–492.
41. Gonze X, et al. (2005) A brief introduction to the ABINIT software package. *Z Kristallogr* 220:558–562.
42. Blanco M, Florez M, Bermejo M (1997) Evaluation of the rotation matrices in the basis of real spherical harmonics. *J Mol Struct THEOCHEM* 419:19–27.